Landsat-swath Imaging Spectrometer Design

Pantazis Mouroulis*, Robert O. Green, Byron Van Gorp, Lori Moore,
Daniel W. Wilson, Holly A. Bender
Jet Propulsion Laboratory, California Institute of Technology, Pasadena, CA 91109, USA

ABSTRACT

We describe the design of a high-throughput pushbroom imaging spectrometer and telescope system that is capable of Landsat swath and resolution while providing better than 10 nm per pixel spectral resolution. The design is based on a 3200 x 480 element x 18 μm pixel size focal plane array, two of which are utilized to cover the full swath. At an optical speed of F/1.8, the system is the fastest proposed to date to our knowledge. The utilization of only two spectrometer modules fed from the same telescope reduces system complexity while providing a solution within achievable detector technology. Predictions of complete system response are shown. Also, it is shown that detailed ghost analysis is a requirement for this type of spectrometer and forms an essential part of a complete design.

Keywords: Imaging spectrometer, Landsat, Dyson spectrometer

1. INTRODUCTION

In their many generations, Landsat satellites have provided a wealth of data for Earth observations that have substantially impacted our understanding of terrestrial natural and anthropogenic processes. This impact is due to the global high-resolution coverage and relatively large number of spectral bands of the Landsat instruments. The combination of Landsat swath and resolution with spectrally contiguous imaging spectrometer data is the next major step in enhancing Landsat utility.

Landsat 8[1] carries the Operational Land Imager (OLI) and the Thermal Infrared Sensor (TIRS). OLI[2] is a replacement of the Thematic Mapper found in previous Landsat generations which uses a scan mirror to cover the required wide swath. OLI instead utilizes long detector arrays in a pushbroom fashion. While the removal of the scan mirror is an advance in terms of signal to noise, reliability and potential simplicity of design, the OLI design still suffers from registration concerns between bands owing to the non-simultaneity of data collection. An imaging spectrometer would not suffer that problem since it is capable of collecting all bands simultaneously. However, it has been generally difficult to find optical spectrometer and system solutions that satisfy the swath, resolution, spectral range, and signal to noise ratio (SNR) of the heritage systems. We present in this paper a pushbroom imaging spectrometer design that can achieve these objectives. Evidently the imaging spectrometer also has the advantage of providing contiguous spectra which enhance material identification beyond the capabilities of multispectral systems.

Any such system design must start from the detector array. We have chosen an array that represents a not-too-great extension of current technology and may be produced in the relatively near future. This is a 3200 x 480 element array with 18μm square pixels that is planned for production by Teledyne Inc. The sensing material is thinned HgCdTe with a spectral response covering the entire 380-2500 nm band. With the addition of an order-sorting filter, this array can provide full spectrum coverage in a grating spectrometer, while two such arrays offering 6400 pixels suffice to cover the Landsat swath of 185km with 30 m sampling.

There have been previous attempts to design similar systems based on alternative detectors. Mouroulis et al[3] suggested a design with stackable modules based on miniature Offner spectrometers, of 720 spatial pixels each, with separate short-wave infrared (SWIR) and visible to near infrared (VNIR) spectrometer channels, consistent with the detector technology of the time. A more compact design that could handle several stacked detectors in a single spectrometer was published by Chrien and Cook[4]. Later, using a monolithic long detector array, Silny and Chrien[5] were able to demonstrate a monolithic wide-field system (CIRCE), albeit limited to the VNIR range and with a small pixel size (8um) that limits throughput. They also performed a system trade study and concluded that a "semi-modular" system utilizing two detector arrays may be the optimum compromise given foreseeable detector technology. They then proposed an optical design concept based on a monolithic array of 18μm pixel size. However, no design performance parameters were published beyond a raytrace schematic.

*pantazis.mouroulis@jpl.nasa.gov; phone 1 818 393-2599;

Lucke and Fisher[6] designed a fast spectrometer system based on the Dyson spectrometer design. However, that system was also limited in spectral range to 1000 nm, and utilized small pixel detector array of 2000 elements, with 10 μm pixel size. As the array size increases to 3200 x 18 μm in our case, the design must change substantially to accommodate this nearly threefold increase in slit length. In addition, their 3.8° field of view (FOV) is a small fraction of our required 16° which cannot be achieved by the Schmidt-Cassegrain telescope of Lucke and Fisher. Finally, stray light computation was not performed for the spectrometer. We show in this paper that stray light computation is an integral part of this type of Dyson spectrometer design where the slit intersects the plane of symmetry and must be successfully performed before a design can be accepted.

2. SPECIFICATIONS

The system specifications are driven not only by the detector size and required orbit/resolution but also by the requirement for high throughput to maximize SNR, as well as high response uniformity to maximize spectral fidelity. The specifications are shown in Table 1. We show only the instrument specifications that are independent of orbit. It may be seen that a 30 m sampling and a 185 km swath are achieved from a 705 km orbit including a small amount of overlap between the two spectrometer modules.

In Table 1, spectral uniformity is a combined measure of the so-called "smile" (curvature of the monochromatic slit image) and the through-field variation of the spectral response function FWHM. The spectral IFOV uniformity is a similarly combined measure of "keystone" (chromatic variation of magnification) and the chromatic variation of the cross-track spatial response function shape. These values have been reduced to fractional pixel errors as explained in Section 5. A value of 100% indicates no error, while a value of 90% indicates a total error equivalent to a smile or keystone of 10% of a pixel (0.18 μm) across the entire field or spectrum.

Table 1. Design specifications

Parameter	**Value**
Scan type	Pushbroom
Cross-track spatial elements	6400 (2 x 3200)
Telescope focal length	420 mm
F-number	1.8
Telescope FOV	16° x 1.3°
Spectrometer magnification	-1
Detector pixel size	18 μm square
Slit length (one spectrometer)	57.6 mm
Spectral range	380 – 2510 nm
Spectral sampling	6.8 nm per 18 μm pixel
SNR	See Fig. 5
Spectral uniformity	90%
Spectral IFOV uniformity	90%

We have chosen to design the system with a more challenging spectral sampling of 6.8 nm relative to the coarser 10 nm of a heritage spectrometer such as AVIRIS[7]. However, we note that the spectral sampling can be increased to 10 nm without any changes to the design beyond the grating pitch. All conclusions drawn below will hold, and the system will look practically identical.

3. OPTICAL DESIGN

The requirements for high speed, large field, and high uniformity can be satisfied with a spectrometer of the Dyson type as will be shown below. The field and aperture requirements of the telescope can be satisfied in one of two ways, either with a two-mirror off-axis design similar to that used in PRISM[8] and similar spectrometers[9], or with a more common three-mirror anastigmat (TMA). The first design requires two 4th order aspheric surfaces and is tolerant to positional misalignments. However, as Fig. 1 shows, the required focal length makes this a very large telescope since it is

effectively an inverted telephoto design. A TMA design retains smaller size at the expense of an extra mirror and higher order aspheric terms on all three mirrors. It has also been found advantageous to let float the location of the telescope aperture stop, so there is not a perfect real stop location in this design. However, we have demonstrated in practice that the lack of a real stop at the telescope is no disadvantage to instrument performance.[8,10]

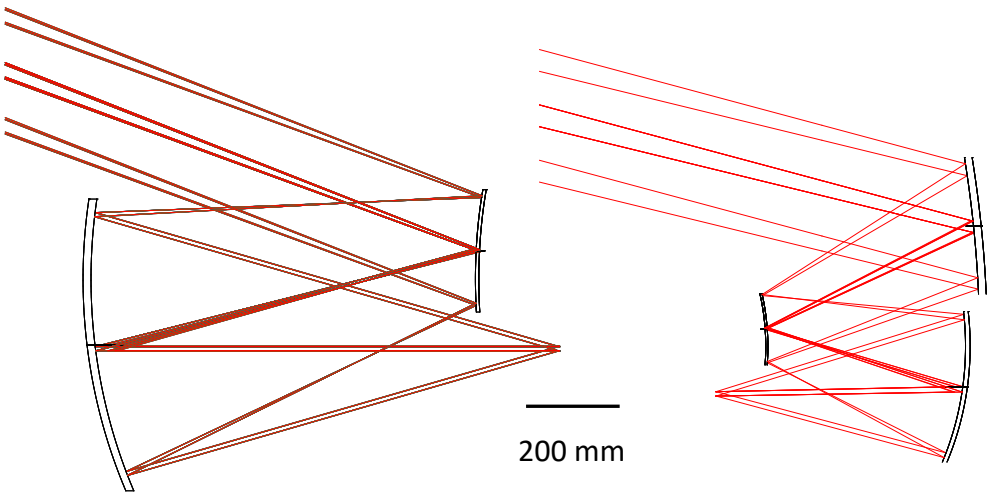

Figure 1. Candidate telescopes, F/1.8, 420mm focal length, 16° x 1.3^0 FOV. The TMA (right) is chosen as the more compact of the two.

The field split is achieved by having the projection of one spectrometer slit ahead of the other in the direction of motion. The angular separation is 1.3O. A larger angular separation makes packaging easier, but extends the field to the point where the imaging performance of the TMA is compromised.

In order to achieve the required performance under these specifications, uncommon for a TMA of this type, small element decenters along the y axis (vertical in Fig. 1) had to be permitted thus breaking the original axial symmetry of the design by a small amount. There is also an additional subtlety in that the two spectrometers are not symmetrically placed about the plane of symmetry of the TMA. Rather, a bias of 2° in object space allows the slit projections to be better located inside the ring of optimum image quality[11]. This has the effect of balancing the field performance in this kind of telescope design which in this case is pushed to its limit. The resulting image coordinates as well as the rms wavefront error achieved are shown in Table 2. The maximum rms spot radius for the worst field was 6.8 □m, but the telescope was optimized for wavefront error rather than spot size.

Table 2. Telescope rms wavefront error

x-field (degrees)	y-field (degrees)	rms wavefront error, waves @633 nm
1	-13	0.15
-4	-13	0.16
-6	-13	0.20
-7	-13	0.32
1	-11.7	0.25
6	-11.7	0.15
8	-11.7	0.17
9	-11.7	0.32

A raytrace of the spectrometer is shown in Fig. 2. It is of the Dyson design[12] with a concave grating and a separated doublet refractive element, comprising CaF_2 and fused silica lenses. The separation, which is on the order of 0.1mm is required due to the thermal incompatibility of the two materials. The CaF_2 front element is further broken down into

three cemented elements, a planoconvex lens, and an input and output reflecting prism, required for detector clearance. The front prism, which operates in total internal reflection, was found necessary to provide clearance for the TMA telescope. This would not have been necessary with the larger two-mirror telescope. The complete system raytrace with both spectrometers is shown in Fig. 3.

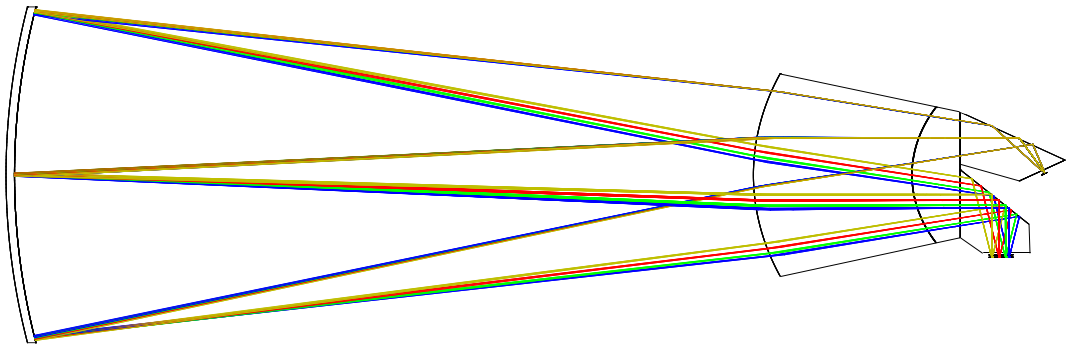

Figure 2. Spectrometer ray-trace in the spectral direction. The two reflecting prisms and planoconvex element are made of CaF_2.

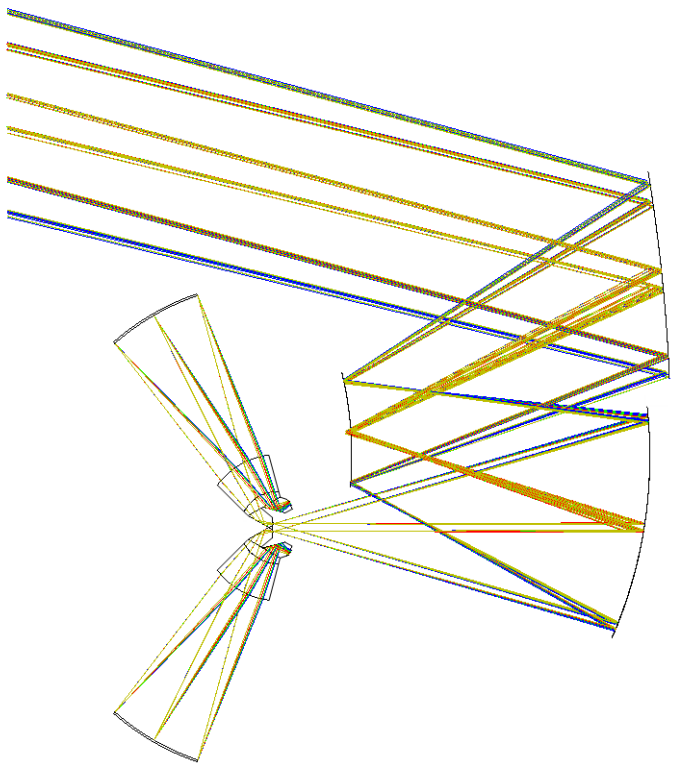

Figure 3. Complete system raytrace with two spectrometers separated in the along-track direction via a roof mirror.

Spectrometer performance and telescope performance are assessed in the next section in terms of predicted system response functions, as well as uniformity. In this section we also provide a measure of optical performance alone which may be more readily appreciated by the optical designer. Since the system is designed for a detector of 18 m pixel size, and since the x and y (or spatial and spectral) directions are conceptually and physically separate, the most relevant

optical performance metric is the x- and y-enclosed (or "enslitted") energy inside the pixel width. This is shown in Table 3 for several wavelengths and only the worst-case field position. In addition, the fraction of the enclosed energy relative to the diffraction-limited case provides an idea of the aberration content in the image. It can be seen from Table 2 that the enclosed energy is everywhere above 85% in absolute terms, and more than 88% of the corresponding diffraction-limited case. In order to achieve this performance over such a wide field and fast optical speed, it has been found necessary to introduce a small conic term to the grating substrate and a 4th order aspheric term to the fused silica lens on the surface facing the grating. Zemax® optical design software was used for the design and analysis.

Table 3. Enclosed energy in 18 μm width (spectrometer only)

Wavelength	x-direction (spatial)	Fraction of diffraction-limited
380	0.94	0.95
630	0.89	0.90
1200	0.85	0.88
2500	0.88	0.94

Wavelength	y-direction (spectral)	Fraction of diffraction-limited
380	0.96	0.97
630	0.93	0.94
1200	0.92	0.94
2500	0.89	0.95

The diffraction grating is 14 cm in diameter and has a radius of 347.3 mm. Advances in grating fabrication by electron beam lithography[13,8] mean that this large grating is now feasible. A grating of 12 cm diameter has already been produced and used in a scaled version of this spectrometer design with a somewhat smaller slit and larger pixel size, with the results due for publication soon.

The grating pitch is a rather coarse 91 μm. The groove design is made to depart from the simple sawtooth profile in order to better distribute the first order diffracted energy in the whole band and achieve a balanced signal to avoid saturation. The predicted grating efficiency is given in Fig. 4. This figure shows the efficiency of many orders, all of which are potentially significant in the stray light computation to be shown below.

4. SYSTEM-LEVEL PERFORMANCE PREDICTIONS

We demonstrate the overall system performance through computed spectral and spatial response functions as used in imaging spectrometer data reduction algorithms. As the Airy disk diameter even for the longest wavelength (2.44*2.5*1.8) is considerably smaller than the pixel and slit width of 18 m, the incoherent approximation is considered adequate, as a more detailed but much more laborious partially coherent computation would only lead to corrections of less than 10%.[14,15] We consider that the slit length is along the x-axis, which means that the spectral direction is the y, as is also the direction of motion. In the incoherent approximation, the Spectral Response Function (SRF) depends only on the spectrometer and can be computed starting at the slit, as the convolution of slit, y-line spread function, grating resolution function and detector pixel response. Thus this is equivalent to flood-illuminating the slit without a telescope. The absence of a real telescope aperture stop and presumed mirror oversizing help approximate that condition closer.

The Along-track spatial Response Function (ARF) is a function of the telescope only and can be computed as the convolution of the telescope y-line spread function with the slit width, and an additional rect function of the same width representing the effect of motion blur (or integration time). Thus this is equivalent to receiving the signal on a photodetector placed immediately behind the slit, while neglecting the spectrometer. However, we approximate the real situation better by analyzing the telescope performance only at the F-number that is accepted by the spectrometer and neglecting the telescope aperture oversize. Finally, the Cross-track spatial Response Function (CRF) is computed as the convolution of the combined telescope and spectrometer system (x-) line spread function with the detector pixel response. It can be seen then that this method of assessment, in addition to being relevant to the data reduction algorithms also provides a complete assessment of the telescope, the spectrometer, and their combination in a physically meaningful way. In the computation, we assume a Gaussian pixel response function with a Full Width at Half Maximum

(FWHM) equal to the pixel pitch. This has been found to be a good approximation to the actual detector response both from direct measurements of the detector MTF and from indirect measurements of the spectrometer system response as above. A small (~10%) increase in the FWHM can be assumed from the longest to the shortest wavelength based on experience with past detector arrays. We choose to neglect that variation here in the absence of specific measurements for the new detector array proposed here.

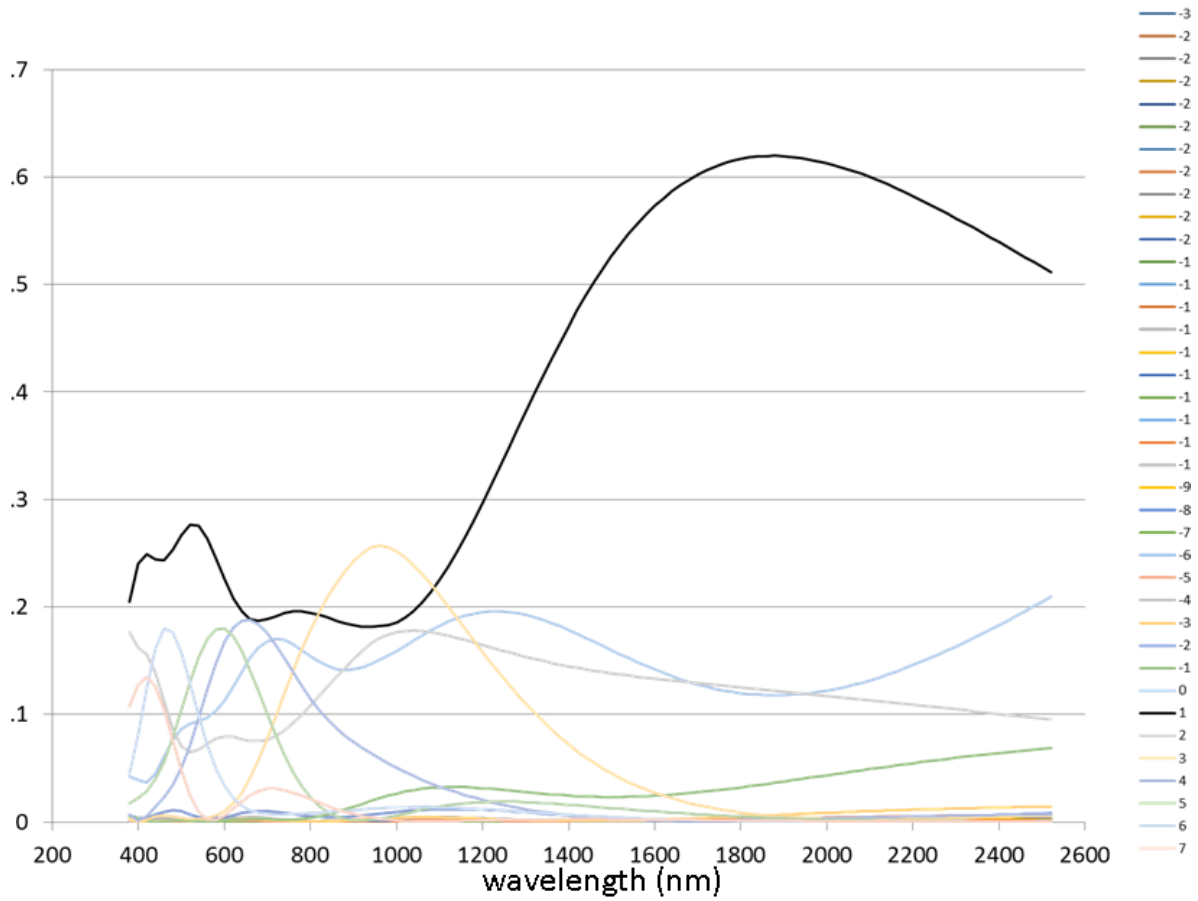

Figure 4. Grating efficiency in orders 7 to -30. The main order is +1. All the positive orders show a high efficiency peak somewhere between 400 and 1400 nm. The zeroth order is the one with the second highest efficiency at 2500 nm. All the negative orders are very small but not negligible in a stray light context. The exception is the -1 order which is the one with the 4th highest efficiency at 2500 nm.

The CRF and SRF shapes are well approximated by a Gaussian function as a consequence of the Gaussian assumption for the pixel response, as well as the fact that the point spread functions are largely contained within a pixel. We have measured such response functions many times in the past and verified a near-Gaussian shape.[8,10] The ARF shape tends to be more triangular due to the convolution of two rect functions, the only smoothing factors being telescope aberrations and diffraction, neither of which is particularly large. Thus the ARF is also a smooth, single-peaked function, and we can choose the FWHM as a simple way of characterizing the width of all response functions. The corresponding variation in FWHM is then a measure of the residual non-uniformity. There are also two additional measures of non-uniformity that describe the geometric alignment of the centroids of the SRF with field (for a given wavelength) and the CRF with wavelength (for a given field position), also known as smile and keystone respectively. In this design, they are controlled at a small fraction of a pixel. The design exhibits a maximum smile value of 2.9% of an 18 □m pixel width (or 0.52 □m in absolute terms) over the full 57.6 mm slit length. This worst-case smile occurs at a wavelength of 1.6 □m. Such small smile values over a long slit length have been demonstrated in practice with an Offner spectrometer.[16] Finally, the design also exhibits negligible amounts of keystone (0.25% of a pixel) over the full spectrum.

The results of the SRF computations are shown in Table 4. It may be seen that the maximum FWHM is 1.44 pixel units and the maximum variation with wavelength, occurring at 1600 nm, is ~4.4%. Thus the maximum spectral non-uniformity, calculated as maximum smile plus ½ of maximum SRF FWHM variation[17] is 5.1% of a pixel. With regards to the validity of the incoherent approximation, we note that the SRF width at the long wavelength will generally be slightly smaller when slit diffraction is taken into account, and that the SRF variation through field is not expected to change appreciably.

Table 4. SRF FWHM through field and wavelength

Distance from center of slit (mm)	FWHM @380 nm (pixel fraction)	FWHM @800 nm (pixel fraction)	FWHM @1600 nm (pixel fraction)	FWHM @2500 nm (pixel fraction)
0	1.31	1.33	1.35	1.42
11.25	1.32	1.35	1.36	1.4
18	1.33	1.38	1.37	1.39
22.5	1.33	1.39	1.38	1.39
28.8	1.33	1.39	1.37	1.44

The results of the CRF computations are shown in Table 5. Two configurations are shown corresponding to the two spectrometers. The difference arises from the variation in telescope performance in the along-track direction (or equivalently, the 1.3° field difference between the two spectrometers in the y-direction. It can be seen that the maximum CRF width is 1.34 pixel units occurring at one edge of the field. The maximum variation through wavelength occurs at -7° for configuration 2 and is approximately 13%. Variation in detector response through wavelength will likely not play a role, but if it did it would be in a beneficial direction as it tends to broaden the response at the shorter wavelengths. The maximum non-uniformity is again calculated as the sum of maximum keystone plus ½ of maximum CRF FWHM variation and is <7%.

Table 5. CRF FWHM through field and wavelength

Configuration 1	CRF FWHM at 1°	CRF FWHM at 6°	CRF FWHM at 8°	CRF FWHM at 9°
380 nm	1.12	1.12	1.09	1.19
800 nm	1.15	1.15	1.13	1.27
1600 nm	1.15	1.11	1.13	1.21
2500 nm	1.21	1.14	1.09	1.16

Configuration 2	CRF FWHM at 1°	CRF FWHM at -4°	CRF FWHM at -6°	CRF FWHM at -7°
380 nm	1.12	1.1	1.13	1.26
800 nm	1.14	1.13	1.12	1.18
1600 nm	1.12	1.11	1.13	1.22
2500 nm	1.19	1.13	1.15	1.34

Representative ARF computation results are shown on Table 6 for both configurations in pixel width units. It may be seen that the maximum ARF is 1.34 and that the maximum variation with wavelength, occurring for configuration 1 and

a field of 1°, is ~7.7%. Thus the system meets the 90% uniformity requirements of Table 1 with sufficient margin to allow for fabrication and assembly tolerances.

Table 6. ARF FWHM through field and wavelength

Configuration 1	ARF FWHM at 1°	ARF FWHM at 6°	ARF FWHM at 8°	ARF FWHM at 9°
380 nm	1.24	1.16	1.21	1.19
800 nm	1.24	1.15	1.23	1.26
1600 nm	1.27	1.16	1.19	1.26
2500 nm	1.34	1.21	1.16	1.17

Configuration 2	ARF FWHM at 1°	ARF FWHM at -4°	ARF FWHM at -6°	ARF FWHM at -7°
380 nm	1.17	1.15	1.25	1.24
800 nm	1.2	1.17	1.27	1.23
1600 nm	1.19	1.16	1.21	1.22
2500 nm	1.25	1.18	1.18	1.33

5. SIGNAL TO NOISE PERFORMANCE

The signal to noise ratio has been calculated through a detailed model that has been validated by several past sensors built at the Jet Propulsion Laboratory. The model accounts for 100 e- noise, 700,000 e- full well, and 4.4 ms integration time. The benchmark radiances come from MODTRAN with the assumption of mid latitude summer atmosphere and a range of surface reflectance and illumination angles as shown in Fig. 5. It may be seen that the unusual grating efficiency curve of Fig. 4 is effective in flattening the SNR through the spectral band.

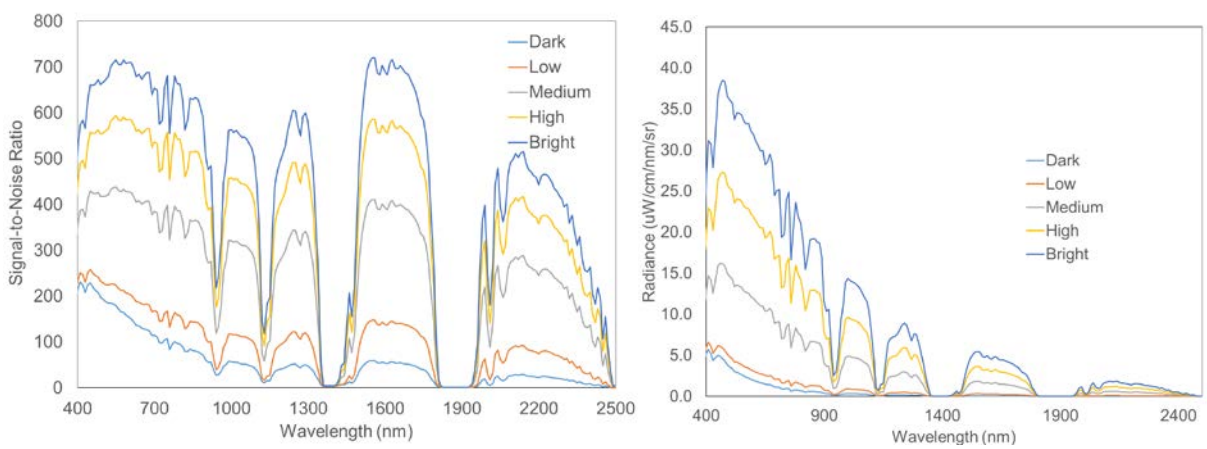

Figure 5. Predicted signal to noise ratio (left) and corresponding reference radiances for the following conditions of (reflectance, sun angle): (0.01, 45°); (0.05, 45°); (0.25, 23.5°); (0.5, 23.5°); (0.75, 0°).

6. STRAY LIGHT PERFORMANCE

Stray light in a grating spectrometer tends to be dominated by grating scatter, which depends significantly on the grating fabrication method. Gratings with low overall scatter and low ghosts have been demonstrated with the electron beam method[13, 18] and gratings made with the method have flown on several instruments and missions.[8, 10, 19-21] In a Dyson-type spectrometer there are additional sources of ghosts that must be carefully controlled through judicious positioning of the slit in combination with the grating dispersion and choice of blazed order. A significant source of stray light is the reflection from the curved surfaces of the Dyson lens assembly. This must be directed away from the detector area even if very good antireflection coatings were available. The broad spectral band of the present design makes it difficult to procure efficient anti-reflection coatings; in the analysis that follows, a 2.5% average surface reflectivity was assumed, which likely represents the limit of what can be achieved with reasonable effort.

The next most significant source of stray light in a Dyson spectrometer arises from reflections from the detector and order-sorting filter. These reflections are directed towards the grating and can be returned to the detector via a different diffraction order. Actually, this situation can occur even in Offner-type spectrometers and we have observed such reflections returned at a very high order (40 or higher), which may still retain non-negligible efficiency. The reflected light forms a spatial ghost at a location symmetric about the image of the center of the slit relative to the original field point. A way to avoid them is to displace the slit so that it lies wholly on one side of the spectrometer plane of symmetry.[22] This however reduces the slit length and therefore field size to only half of what the spectrometer can otherwise handle, and for a wide-field (or equivalently long-slit) system such as sought here, it is not a desirable solution as it would increase the size of the spectrometer beyond reasonable limits.

Assessment of the impact and intensity of these ghosts requires a detailed analysis, which must use realistic values for detector and filter reflectivity, as well as grating efficiency in all the potential returning orders. It is not possible to draw quick conclusions without such an analysis, because of the number of orders and combinations involved. It is also to be noted that light returned in a higher order is dispersed accordingly. This means that we cannot use isolated (sparsely sampled) wavelengths as the input to the stray light model. Rather, we must input a wavelength band per pixel even though such band may not be resolvable in the first order. We have used six individual wavelengths per 6.8 nm band. If appropriately centered, these six wavelengths will all fall on a single pixel in the first (blazed) order, but will be dispersed further when returning through a higher order. This gives a better estimation of the power of a ghost reflection relative to the first order.

The stray light analysis considers specular light only. This is the most important part of the analysis; regarding scattered light, the largest contribution is from the grating, however gratings have distinct and individual scatter characteristics that are normally only established through measurement. In any case, the specular ghost contribution overwhelms the grating scatter unless care is taken to reduce or avoid it. It is therefore this deterministic first part of the stray light analysis that must be tackled at the design stage.

The grating orders that are involved in the computation are from -30 to 7. All these orders contribute to stray light via a reflection from the detector/OSF assembly that can return after a second diffraction from the grating. A detailed table of efficiency through wavelength for all these orders is used, derived from PCGrate® software by inputting the groove shape and other grating parameters. Other model assumptions include: 95% reflectivity of the OSF rejection bands, 2.5% average reflection on the non-filter surface as well as all other refractive surfaces, 10% reflectivity of detector surface independent of wavelength, a black mask coating surrounding the OSF with a conservative 10% spectrally flat reflectivity. The OSF segments are a low pass up to 740 nm, a bandpass up to 1400 nm, and a high pass up to 2500 nm. We have also used a realistic slit model, based on a black Si slit assembly such as demonstrated in the PRISM instrument, with a small flat area surrounding the slit that has the reflectivity of gold. We have used FRED® for these computations.

A typical example of a computation for a single waveband centered at 380 nm is shown in Fig. 6, where the spatial direction is horizontal. The figure shows a strong peak at the first order location on the bottom left. To the right, symmetrically placed with respect to the middle of the slit is the ghost reflection from the detector/OSF assembly. Around the first order peak we see stray light arising from multiple reflections in the various elements and the OSF. This is sharply delimited by the next filter segment which rejects these wavelengths. Above the main first order peak and near the filter boundary we also observe the glow from the second order, which passes through the first segment but gets cut

off by the second. Further up in the spectral direction we see the 380 nm band in higher orders being mostly rejected by the OSF, which still has a small residual transmission (1E-4).This is a typical rejection level that manufacturers can achieve and is considered adequate, so this residual high order transmission is of no concern. The spatial ghost arising from this wavelength band is on the order of 1E-5 relative to the peak. It is weak thanks to the choice of slit location relative to grating pitch and order. However, this may not be the only wavelength band contributing to a spatial ghost at that location. This is examined further below.

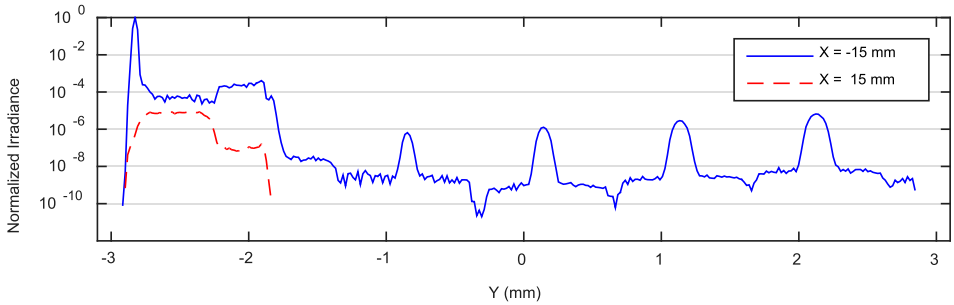

Figure 6. Example of spatial ghost at an incident wavelength of 380 nm. Top: distribution at the detector. Bottom: traces along the y axis at x = -15 mm (main image) and at x = 15 mm (ghost image), show the relative magnitude and dispersed nature of the ghost. Also note that the higher order peaks get progressively dispersed indicating that a wavelength band, rather than a single wavelength, is being traced.

The computation for a distinct spectral band was repeated in order to cover the entire spectral range, thus forming effectively the image of a point of white light. The result is shown in Fig. 7. It can be seen that the sum of all spatial ghosts is at the level of 1E-4 of the main order. It should be clearly understood that this low level is not an automatic result for all Dyson spectrometers, but rather, a consequence of specific design choices regarding the slit location, spectrometer size, and grating pitch and order. An example of a spectrometer with higher level of ghost light (albeit minimum for the particular size and dispersion) is given in ref. 23.

The next stage of assessment is to show the image of an extended spatial object. This was performed for an object of length equal to half the slit and every wavelength in turn. Subsequently, these results are all added to produce an image of a white-light object with a length of half the slit. The resulting distribution is shown in Fig. 8. It may be seen that the stray light remains below the 1E-3 level everywhere. This is at or below the level of expected grating scatter and thus can be considered satisfactory. Since this is a deterministic model that depends on verifiable assumptions, we expect the prediction to hold quite closely and be conservative especially when accounting for the possibility of much lower detector reflectivity through a linear variable A/R coating that is now under development at Teledyne under a different program.[24]

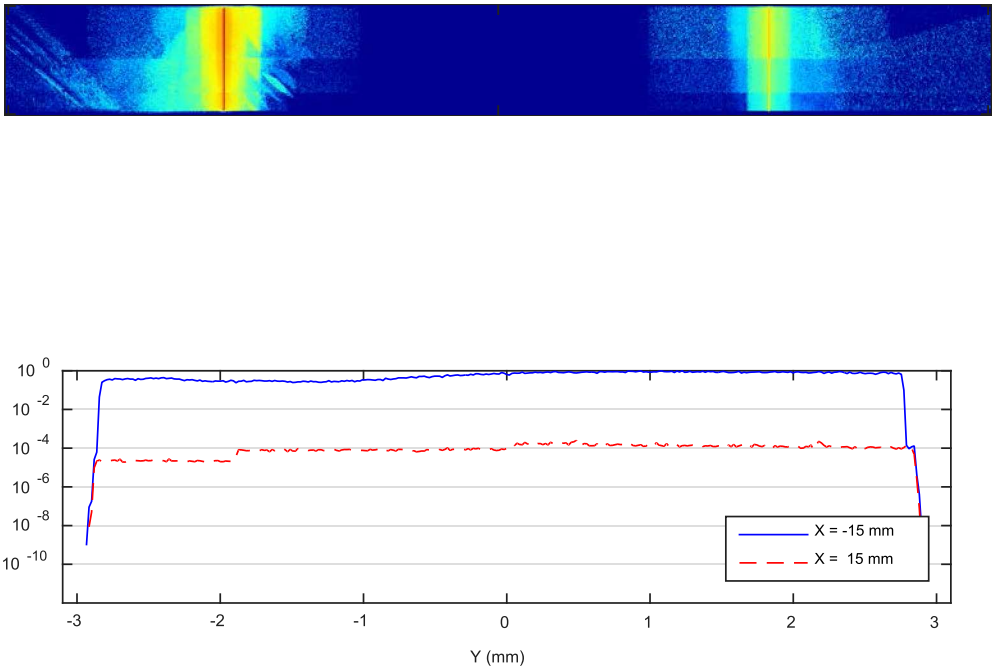

Figure 7. Top: Image of white light point, with all wavelengths equally weighted. Bottom: Irradiance along the spectral axis at x = -15 mm and x = 15 mm (ghost image). The main image at -15 mm effectively follows the first order grating efficiency and is normalized to unity at the peak. The ghost image remains at about 1E-4 at any given spectral location.

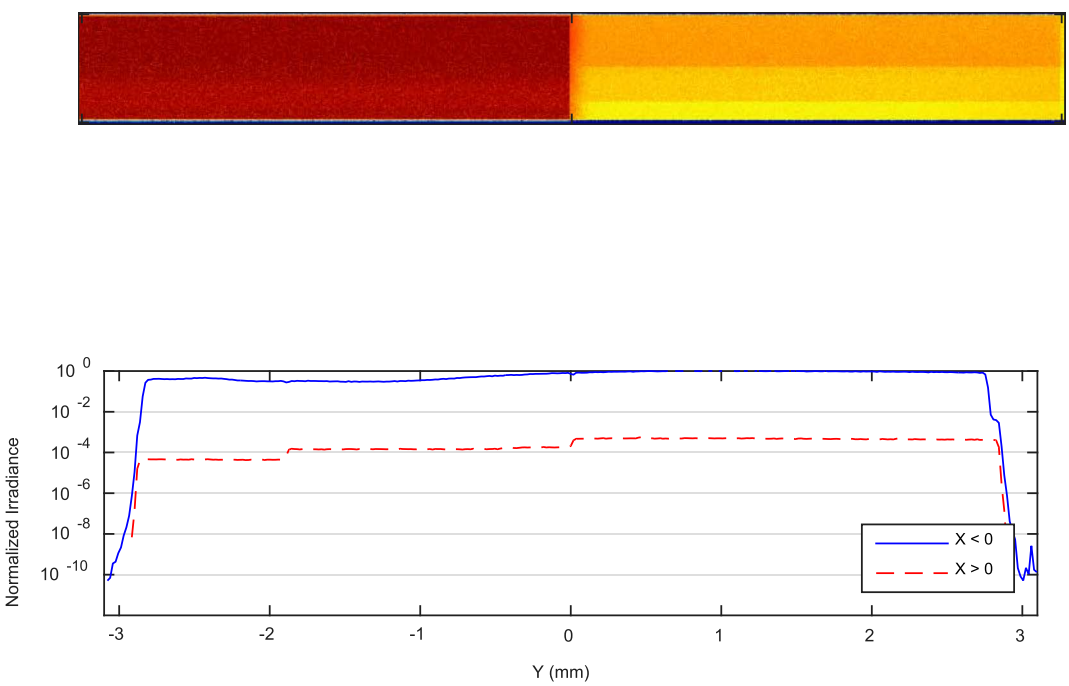

Figure 8. Top: Image of a white light object filling half the slit Bottom: Traces along the spectral axis.

7. TOLERANCING AND FABRICATION

Some comments must be made regarding tolerancing and fabrication of the design. The rather extreme properties of this design raise the question of whether they can be achieved in practice. Although we do not present a tolerancing analysis here, we note that we have fully analyzed and have nearly completed the fabrication of a scaled model that is about 85% of the size of the present design.[25] The tolerancing analysis performed there revealed all fabrication tolerances to be within typical range for precision quality optics. All elements for that model have been fabricated and passed inspection. The most critical part of the assembly is the relative alignment and bonding of the CaF_2 and SiO_2 lens elements to the structure. A centering method utilizing shims, an air-bearing stage, and quadrant detectors to detect misalignment/wedge was developed and used to align the two lenses and bond them in their mounts successfully and within tolerance. A full mechanical design has also been performed and parts fabricated, with full assembly due soon. A grating mount that permits fine clocking as well as lateral translation has already been tested in the PRISM instrument and its characteristics would fully satisfy the present requirements. Similarly, PRISM demonstrated how the detector assembly can be placed in close proximity to the slit (~ 2mm clearance, tighter than the present design). Finally, we have tested the transmittance of optical cements and have found a suitable cement with very little absorption over the full spectral range of 380-2500 nm over two transmissions. Therefore we expect that this system can be built as designed.

8. CONCLUSIONS

We have presented and analyzed a high-throughput and high uniformity optical design that can achieve Landsat swath and resolution using two spectrometer modules in a pushbroom scan, coupled to a three-mirror anastigmat telescope operating at F/1.8. The system was analyzed in terms of optical enclosed energy, system-level spatial and spectral response functions, predicted signal to noise ratio from orbit, and stray light performance due to ghost reflections. Feasibility is supported by analysis and prototype development.

ACKNOWLEDGMENTS

This research was performed at the Jet Propulsion Laboratory, California Institute of Technology under a contract with the National Aeronautics and Space Administration. Reference herein to any specific commercial product, process, or service by trade name, trademark, manufacturer, or otherwise, does not constitute or imply its endorsement by the United States Government or the Jet Propulsion Laboratory, California Institute of Technology.

REFERENCES

[1] https://lta.cr.usgs.gov/L8

[2] Irons, J.R., J. L. Dwyer, J. A. Barsi.: "The next Landsat satellite: The Landsat Data Continuity Mission" Remote Sens. Environ. 122, 11–21 (2012)

[3] Mouroulis, P., D. A. Thomas, T. G. Chrien, V. Duval, R. O. Green, J. J. Simmonds, A. H. Vaughan: "Trade Studies in Multi/hyperspectral Imaging Systems, Final Report" (1998), http://esto.nasa.gov/files/1999/Mouroulis.pdf

[4] Chrien, T.G., and L. G. Cook: "Design Concept for a Landsat-Class Imaging Spectrometer with well Corrected Spectral Fidelity", Proc. SPIE 5157, 90-97 (2003)

[5] Silny, J.F., and T. G. Chrien: "Large format imaging spectrometers for future hyperspectral Landsat mission", Proc. SPIE 8158, 815803 (2011)

[6] Lucke, R., and J. Fisher: "The Schmidt-Dyson: A fast, space-borne wide-field hyperspectral imager", Proc. SPIE 7812, 78120M (2010)

[7] Green, R.O., M. L. Eastwood, C. M. Sarture, T. G. Chrien, M. Aronsson, B. J. Chippendale, J. A. Faust, B. E. Pavri, C. J. Chovit, M. Solis, M. R. Olah, and O. Williams: "Imaging spectroscopy and the Airborne Visible/Infrared Imaging Spectrometer (AVIRIS)", Remote Sens. Environ. 65, 227-248 (1998)

[8] Mouroulis, P., B. Van Gorp, R. O. Green, H. Dierssen, D. W. Wilson, M. Eastwood, J. Boardman, B.C. Gao, D. Cohen, B. Franklin, F. Loya, S. Lundeen, A. Mazer, I. McCubbin, D. Randall, B. Richardson, J. I. Rodriguez, C. Sarture, E. Urquiza, R. Vargas, V. White, K. Yee: "Portable Remote Imaging Spectrometer coastal ocean sensor: design, characteristics, and first flight results", Appl. Opt. 53, 1363-1380 (2014)

[9] Mouroulis, P., B. Van Gorp, V. E. White, J. M. Mumolo, D. Hebert, M. Feldman: "A compact, fast, wide-field imaging spectrometer system", SPIE Proc. 8032, 80320U (2011)

[10] Bender, H.A., P. Mouroulis, M. L. Eastwo1.od, R. O. Green, S. Geier, E. B. Hochberg: "Alignment and characterization of high uniformity imaging spectrometers", Proc. SPIE 8158, 81580J-1 (2011)

[11] Korsch, D., [Reflective Optics], Academic Press (1991)
[12] Mertz, L.: "Concentric spectrographs", Appl. Opt. 16, 3122-3124 (1977)
[13] Wilson, D.W., P. D. Maker, R. E. Muller, P. Mouroulis, and J. Backlund, “Recent advances in blazed grating fabrication by electron-beam lithography,” Proc. SPIE 5173, 115–126 (2003)
[14] Mouroulis, P., R. G. Sellar, J. J. Shea, D. W. Wilson, R. O. Green: “Optical design of a compact imaging spectrometer for planetary mineralogy”, Opt. Eng. 46, 063001 (2007)
[15] Mouroulis, P., and R. O. Green: “Spectral response evaluation and computation for pushbroom imaging spectrometers”, Proc. SPIE 6667, 66670G (2007)
[16] Bender, H.A., P. Mouroulis, R. J. Korniski, R. O. Green, D. W. Wilson: “Wide-field imaging spectrometer for the Hyperspectral Infrared Imager (HyspIRI) mission”, Proc. SPIE. 9222, 92220E (2014)
[17] Green, R.O.: "Spectral calibration requirement for Earth-looking imaging spectrometers in the solar-reflected spectrum", Appl. Opt. 37, 683-690 (1998)
[18] Mouroulis, P., D. W. Wilson, P. D. Maker, R. E. Muller: “Convex grating types for concentric imaging spectrometers”, Appl. Opt. 37, 7200-7208 (1998).
[19] Pearlman, J.S., P. S. Barry, C. C. Segal, J. Shepanski, D. Beiso, and S. L. Carman: “Hyperion, a Space-Based Imaging Spectrometer”, IEEE Trans. Geosci. Rem. Sens. 41, 1160-1173 (2003)
[20] Murchie, S. L. et al: “CRISM (Compact Reconnaissance Imaging Spectrometer for Mars) on MRO (Mars Reconnaissance Orbiter)”, Proc. SPIE 5660, 66-77 (2004)
[21] Simi, C., E. Reith, F. Olchowski: “The mapping reflected-energy sensor-MaRS: a new level of hyperspectral technology”, Proc. SPIE. 7457, 745703. (2009)
[22] Van Gorp, B., P. Mouroulis, D.W.Wilson, and K. Balasubramanian: “Polarization and stray light considerations for the Portable Remote Imaging Spectrometer (PRISM)”, Proc. SPIE 7812, 78120R (2010)
[23] Mouroulis, P., B. Van Gorp, R. O. Green, D. W. Wilson, “Optical design of a CubeSat-compatible imaging spectrometer,” Proc. SPIE 9222, 92220D (2014)
[24] Bender, H.A., P. Mouroulis, C. D. Smith, C. H. Smith, B. Van Gorp, M. L. Eastwood, J. Gross: “Snow and Water Imaging Spectrometer (SWIS): optomechanical and system design for a CubeSat-compatible instrument”, Proc. SPIE in press (2015)
[25] Van Gorp, B., P. Mouroulis, D. W. Wilson, R. O. Green: “Design of the compact wide swath imaging spectrometer (CWIS)”, Proc. SPIE 9222, 92220C (2014)